AGU ADVANCING EARTH AND SPACE SCIENCE

Earth and Space Science

RESEARCH ARTICLE
10.1029/2021EA002046

Special Section:
China-France Oceanography Satellite(CFOSAT): Scientific Applications

Sea-Ice Detection From Near-Nadir Ku-Band Echoes From CFOSAT/SWIM Scatterometer

Charles Peureux[1], Nicolas Longépé[2], Alexis Mouche[3], Céline Tison[4], Cédric Tourain[4], Jean-Michel Lachiver[4], and Danièle Hauser[5]

[1]Collecte Localisation Satellites, Plouzané, France, [2]Φ-Lab Explore Office, ESRIN, European Space Agency (ESA), Frascati, Italy, [3]Ifremer, Laboratoire d'Océanographie Physique et Spatiale, University Brest, CNRS, Brest, France, [4]Centre National d'Études Spatiales, Toulouse, France, [5]Université Versailles Saint-Quentin en Yvelines, Sorbonne Université, CNRS, LATMOS, Paris, France

Abstract SWIM on board CFOSAT is the first spaceborne, low incidence, rotating scatterometer, aiming at measuring in near-real time ocean waves spectra. With five off-nadir beams at incidences between 2° and 10° plus one nadir beam, it covers the Earth in 13 days, including polar regions thanks to its polar orbit. This work aims at exploiting SWIM data over ice regions with two objectives. An off-nadir data-based sea-ice flag is here proposed that allows, first, to eliminate sea-ice polluted echoes for improving the wave spectrum retrieval, and second, to open perspectives for application of sea-ice monitoring with near-nadir Ku-band active sensors. To this end, the signature of both open water and sea-ice radar backscatter is parameterized into Geophysical Model Functions. Then, comparisons with observed profiles through a Bayesian scheme provide a probability of sea-ice presence. After comparison with both model (ECMWF-IFS) and radiometer (SSMI) derived reference data sets, the proposed flag is found to be ready for operational use. At latitudes greater than 40° in absolute value, the proposed flagging algorithm exhibits accuracies of approximately 98% for all beams compared to SSMI data. Beam to beam performances are characterized and show potential for the characterization of sea-ice at Ku-band.

Key Points:

- For the first time, sea-ice is detected globally from Ku-band off-nadir up to 11° incidence thanks to the SWIM/CFOSAT data sets
- Fully analytical Geophysical Model Functions are derived for the Normalized Radar Cross-Section over open water and sea-ice
- A comparison of this new sea-ice flag with SSMI ice concentration shows a high accuracy of our algorithm

Correspondence to:
C. Peureux,
cpeureux@groupcls.com

Citation:
Peureux, C., Longépé, N., Mouche, A., Tison, C., Tourain, C., Lachiver, J.-M., & Hauser, D. (2022). Sea-ice detection from near-nadir Ku-band echoes from CFOSAT/SWIM scatterometer. *Earth and Space Science*, *9*, e2021EA002046. https://doi.org/10.1029/2021EA002046

Received 26 SEP 2021
Accepted 6 JAN 2022

Author Contributions:
Investigation: Charles Peureux
Methodology: Nicolas Longépé
Project Administration: Céline Tison, Cédric Tourain, Jean-Michel Lachiver
Writing – original draft: Charles Peureux
Writing – review & editing: Alexis Mouche, Cédric Tourain, Danièle Hauser

1. Introduction

The CFOSAT program (Hauser et al., 2016) is carried out through a cooperation between the French and Chinese Space Agencies (CNES and CNSA, respectively). Its primary objective is the characterization of the ocean surface to better model and predict the ocean states and improve the knowledge in ocean/atmosphere exchanges. The CFOSAT satellite was launched on October 29, 2018 on a sun synchronous repetitive orbit with a 13-day cycle. Its altitude and inclination are respectively 520 km and 97.4°. Two scientific Ku-Band radars with new technical concepts are embarked on-board the satellite: SWIM, a nadir and near-nadir wave scatterometer (Hauser et al., 2017) and SCAT, a wind fan-beam scatterometer (Xiaolong et al., 2010). Thanks to SWIM, directional ocean waves spectra are produced systematically for the very first time, with a real-aperture scanning radar system (Hauser et al., 2021). SWIM operates at small incidence angles from 0° to 10°, contrary to other in-flight scatterometers (ASCAT, QuikSCAT,…) which are at higher incidence angles.

Since its launch, the CNES Wind and Wave Instrument Center (CWWIC) has generated in Near Real Time (NRT), i.e., less than 3 hr from the measurement, SWIM products of levels 0, 1A, 1B, and 2. SWIM L1B and L2 products are freely available since April 25, 2019 on the AVISO + website (https://www.aviso.altimetry.fr/en/home.html), after a commissioning and calibration period. All the SWIM products are clearly focused on the ocean. With the simultaneous observation of oceanic wind and wave fields, the primary objectives are definitely oriented toward a better understanding of ocean physics and climates, marine meteorology and all associated applications (Hauser et al., 2017). Nonetheless, CFOSAT also offers an opportunity to provide data for the estimation of land surface parameters and polar ice sheet characteristics as both payloads acquired data on all kinds of surfaces. Normalized Radar Cross-Section (NRCS) are provided over all surfaces in the L1 products, opening great opportunities for specific studies and potential products upgrade or complement.

The study presented here focuses on sea-ice. Sea-ice represents approximately from 7% to 15% of the ocean surface. Its study is important for observing and modeling the global warming, especially due to the interaction of sea-ice with atmosphere and ocean (Johannessen et al., 2007; Shokr & Sinha, 2015), and economic activities enhancement (fisheries, freight transport). Our goal is twofold: improve wave products in the marginal ice zone

and exploit SWIM data over sea-ice to get additional information on its characteristics (extension, thickness, age, etc.). Furthermore, a good discrimination between open water and sea-ice covered areas would allow to further study the evolution of waves in the vicinity of the sea-ice pack.

Thanks to its original viewing angle configuration, SWIM complements other existing concepts such as altimetry, scatterometry or radiometry. As far as scatterometers are concerned, sea-ice was extensively studied, mostly at much larger incidence angles (typically above 30°) to detect and characterize sea-ice and icebergs. Girard-Ardhuin and Ezraty (2012) merged passive (SSMI) and active (ASCAT) data into a sea-ice drift product using a maximum cross-correlation method. Lots of sea-ice classification works have been performed on ASCAT and QuikSCAT data, especially allowing the distinction between multiyear and first-year ice (MYI and FYI; Kwok, 2004; Lindell & Long, 2016a, 2016b). The synergy between radiometer and scatterometer allows for even better sea-ice characterization (Lindell & Long, 2016a, 2016b). For example, Zhang et al. (2019) merged ASCAT, QuikSCAT, AMSR, and SSMI data on the 2012–2017 period, flagging open water from the radiometer brightness temperatures, and using machine-learning algorithms to detect clustering resulting from different sea-ice types over the combination of brightness temperatures and NRCS. Belmonte Rivas et al. (2018) were able to estimate sea-ice extents from the combination of ERS, QuikSCAT, and ASCAT scatterometer data from 1992 to 2018.

The ice induces a clear change in the radar backscattering, not only in its level, but also in the shape of NRCS profiles with incidence. Near-nadir, specular reflexions with facets oriented toward the instrument are considered as the main contributors to the radar backscatter (Barrick & Peake, 1968). From this perspective, open water and sea-ice covered areas NRCS profiles inherently differ: while open water has high coherence roughness, dominated by cm-wave length ocean waves, sea-ice roughness is more randomly distributed and its echoes vanish faster with greater incidence. At nadir, sea-ice reflects more energy than open water surfaces, but this tendency switches at slightly more off-nadir angles, where both the contribution from surface and volume scattering need to be taken into account (Remund & Long, 2003). Especially, the radar backscatter of sea-ice decreases very fast with incidence angle (Giles et al., 2007; Kurtz et al., 2013), while open water surfaces generally maintain a certain number of specular reflexion points due to its generally larger correlation length, especially caused by the wavy nature of its surface geometry. Although most mechanisms building up the sea-ice backscatter are known (Landy et al., 2019), the variability of sea-ice physical characteristics make it complicated to summarize the NRCS behavior into a simple parametric model, contrary to the open water case. The analysis of the NRCS profiles is interesting not only for separating sea-ice from open water, but also potentially for characterizing the ice itself (in particular ice age), thanks to its relation with sea-ice roughness.

In this study, a Bayesian approach is selected. Sea-ice detection and characterization is particularly suited to machine-learning based algorithms (Alhumaidi et al., 1997; Zhang et al., 2019), but this approach, although quite efficient, has the disadvantage of remaining a black box. More classical approaches are also usual, especially Bayesian ones (Belmonte Rivas et al., 2012; Belmonte Rivas & Stoffelen, 2011; Breivik et al., 2012; Lindell & Long, 2016a, 2016b; Meier & Stroeve, 2008; Otosaka et al., 2018). Most of them consist in designing a statistical estimator building up on the difference between open water and sea-ice Geophysical Model Functions (GMFs). Over open water, near-nadir Ka/Ku-band GMF are now well established both theoretically (Boisot et al., 2015; Chapron et al., 2000) and empirically (Guerin et al., 2017; Tran et al., 2007), especially for missions TRMM (Freilich & Vanhoff, 2003) and GPM (Chu et al., 2012; Gressani et al., 2018; Hossan & Jones, 2021; Nouguier et al., 2016; Yan et al., 2019). In this study, we propose for the first time, a global characterization of the sea-ice backscatter from near-nadir Ku-band observations. Preliminary studies had been performed on GPM data (Mouche et al., 2015), followed by more quantitative results at regional scale (Karaev et al., 2021; Panfilova et al., 2020). The SASS scatterometer on-board Seasat mission is also worth mentioning, operating in Ku-band, from which sea-ice backscatter is characterized (Swift, 1999), but at slightly higher incidence angles than SWIM (above 23°).

The present study analyzes and demonstrates the possibility to distinguish sea-ice from open water based on SWIM data solely at the range gate resolution. After the description of data used for the study in Section 2, the algorithm is described and illustrated over a test case in Section 3. The resulting flag is then compared to other reference data and discussed in Section 4.

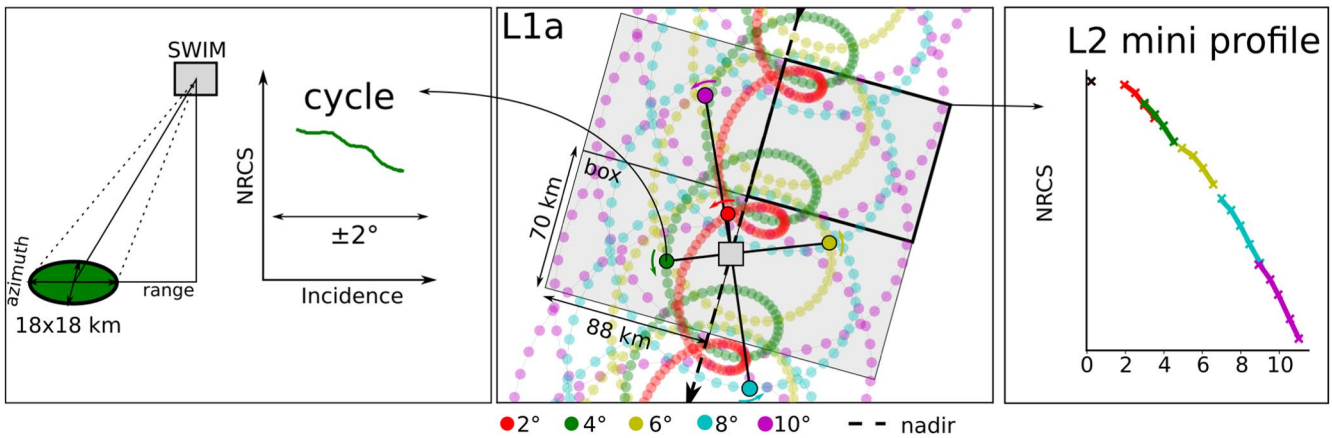

Figure 1. Schematic of SWIM products used in this study. SWIM footprint (left panel) is an approximately 18 km diameter disc, with range incidences centered on the beam nominal incidence, and spanning ±2° at most around it. Such Normalized Radar Cross-Section (NRCS) profile acquisition sequence is called *cycle*. Then (center panel), each beam is illuminated successively in a sequence called *macrocycle*. Along SWIM path, macrocycles are repeated, leading to such cycloid-type periodic pattern. SWIM swath is periodically divided into 70 × 88 km boxes, over which NRCS profiles averages (right panel), the so-called *miniprofiles* are performed at level 2.

2. Data

2.1. SWIM Data

SWIM NRT level 1 (L1) and 2 (L2) products provided by the CWWIC are used for the present study (Hauser et al., 2021). A description of SWIM products used for this study is provided in Figure 1. Calibrated and georeferenced NRCS for each off-nadir beam (2°, 4°, 6°, 8°, and 10° central incidence) are delivered in the L1a products. The L1a algorithm inverts the radar equation to compensate for all instrument gains and losses and for the radar geometry. The mean thermal noise is also accounted in this inversion. The NRCS is then computed for each radar gate in all available azimuths. Note that along this study, all NRCS values are corrected from atmospheric effects (both L1a and L2). Atmospheric corrections are also embedded in SWIM auxiliary products. At a given beam central incidence θ_i, incidence angles range from $\theta_i - 2°$ to $\theta_i + 2°$, except for the 10° beam, for which the incidence only runs up to 11°. The NRCS values analyzed here are provided within the 3 dB footprint in elevation around θ_i. The theoretical radar range resolution is 0.47 m (see Hauser et al., 2017 or Hauser & Tison, 2018), which correspond, after the on-board processing, which includes range gates averaging, to the horizontal resolutions given in Table 1. Due to oversampling applied in the real time on-board processing, this is 1.25 times greater than the range pixel spacing of the L1 products used here.

Note that these NRCS observations although discretized at a fine scale in the elevation direction, are integrated over about 18 km in the direction perpendicular to the elevation plane. Alternatively, the L2 products proposes a simplified information which consists in mean profiles of NRCS with incidence, estimated as averaged values over incidence bins of 0.5° and azimuth bins of 15° over the geographical boxes presented in Figure 1. This variable is called *miniprofile*. L1a products being quite expensive in storage space, L2 *miniprofiles* are more convenient to handle when dealing with data sets spanning several months or years. Here, when dealing with L2 profiles, we work on NRCS profiles averaged azimuthally over 15° and in incidence over 0.5°.

Table 1
Table of Theoretical Horizontal Resolutions for Each Beam Central Incidence

Incidence angle θ_i	Horizontal resolution
2°	53.7 m
4°	26.9 m
6°	9.0 m
8°	10.1 m
10°	8.1 m

NRCS profiles come together with Earth's surface state variables such as land-sea mask LSM, significant wave height H_S, 10 m wind speed U_{10}, sea-ice concentration SIC and sea-surface temperature SST. They are obtained from colocation and interpolation from a 6-hourly ECMWF high resolution forecast, with approximately 9 km resolution. For the present study, version 5.1.2 processed SWIM data is used both for the GMFs computation and the flag validation. Only data from March 2020 to March 2021 are used here. Particular subsets are used either for GMF design or for flag validation. This is precised further down at each step.

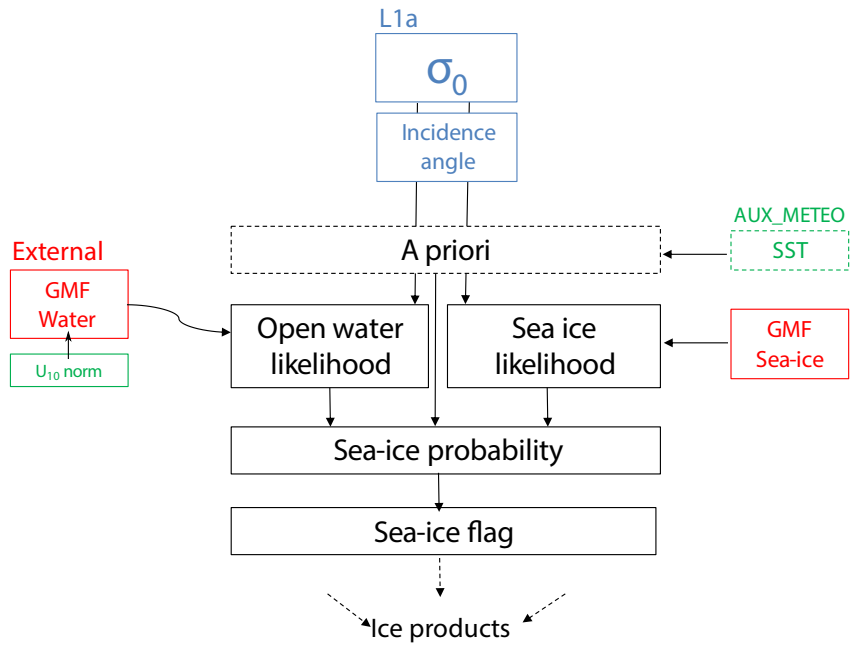

Figure 2. SWIM sea-ice flagging algorithm summary. A Normalized Radar Cross-Section and incidence angle pair from L1a products are compared to Geophysical Model Functions (GMFs) both assuming either sea-ice or open water thanks to a likelihood estimate, given the measurement context (wind speed, beam number, etc.). A prior probability based on sea-surface temperature is combined to the likelihoods into a Bayesian scheme, from which a probability is derived and translated into a binary flag.

2.2. Other Data

Microwave radiometer derived sea-ice concentration data from SSMI are used as reference for the validation of the sea-ice flagging algorithm. SSMI constellation covers the Earth's surface in almost 1 day. Especially, high resolution (12.5 km) brightness temperature data are retrieved and processed by Ifremer CERSAT into daily maps of sea-ice concentration over both the Arctic and Antarctic over stereopolar grids (Ezraty et al., 2007; Kaleschke et al., 2001).

Sentinel-1 NRCS extrawide swath images are also used for comparison. Sentinel-1 is a C-band Synthetic Aperture Radar providing high resolution (GRDM products, 40 m) NRCS images in dual polarization at incidence angles between 19° and 47°.

However, due to their limited spatial and temporal resolutions, the previous references must be analyzed with a critical eye, especially in the marginal ice zone, where sea-ice spatiotemporal variability can be significant (drift, melt, break-up by ocean waves, etc.).

3. Algorithm Description

The sea-ice flagging algorithm is summarized in Figure 2. By definition, the sea-ice flag is activated when the probability of sea-ice presence $P(\text{ice})$ exceeds 0.5:

$$\text{flag} = H[P(\text{ice}) - 0.5] \times (1 - \text{LSM}), \tag{1}$$

where H is the Heaviside function:

$$H(x) = \begin{cases} 1 & \text{if } x > 0 \\ 0 & \text{otherwise} \end{cases}, \tag{2}$$

and LSM is the land-sea mask (1 over land and 0 elsewhere), so that the flag equals one in the presence of sea-ice and 0 elsewhere, especially on land. Note that the land-sea border may sometimes not coincide with coastlines. Especially around Antarctica, for example, in the Ross and Weddel Sea, glaciers or areas of long-lasting continental ice LSM is set to 1 (continent). The introduction of this LSM correction prevents them to be detected as open water.

Sea-ice flagging can be formulated as a Bayesian hypothesis testing problem. The probability of presence of sea-ice is decomposed into conditional probabilities. Given a value σ of the NRCS, the probability of sea-ice presence is $p(\sigma|\text{ice})$. Assuming that the only alternative to *sea-ice* is *open water*, the maximum a posteriori estimator of sea-ice presence is:

$$P(\text{ice}) = \frac{p(\text{ice}|\sigma)}{p(\text{ice}|\sigma) + p(\text{water}|\sigma)}, \tag{3}$$

which compares the two alternative posterior probabilities corresponding other to *sea-ice* or *open water*. The log-likelihood is defined by

$$\mathcal{L} = \ln\left[\frac{p(\text{ice}|\sigma)}{p(\text{water}|\sigma)}\right] \tag{4}$$

so that

$$P(\text{ice}) = \frac{1}{1 + e^{-\mathcal{L}}}, \tag{5}$$

and, using Bayes rule

$$p(\text{x}|\sigma) \propto p(\sigma|\text{x})p(\text{x}), \tag{6}$$

where x is the hypothesis of either sea-ice or open water presence, we have

$$\mathcal{L} = \ln\left[\frac{p(\sigma|\text{ice})}{p(\sigma|\text{water})}\right] + \mathcal{L}_{\text{prior}}, \tag{7}$$

where $p(\sigma|\text{ice})$ and $p(\sigma|\text{water})$ are the likelihoods and the prior log-likelihood is

$$\mathcal{L}_{\text{prior}} = \ln\left[\frac{p(\text{ice})}{p(\text{water})}\right] \tag{8}$$

where $p(\text{ice})$ and $p(\text{water})$ are the a priori probabilities. Comparing $P(\text{ice})$ to 0.5 in order to flag sea-ice contaminated data is equivalent to comparing $\mathcal{L}$ to 0.

The Bayesian approach allows for the proper accounting of an a priori knowledge. Indeed, in order to avoid spurious sea-ice detection at low latitudes, a latitude dependent prior can be defined, that will be discussed in Section 3.1. Then, the likelihood can be estimated from an empirical knowledge of the NRCS distribution (GMF). Here, we propose to first parametrize the mean behavior of NRCS (GMF), then quantify the uncertainty that needs to be allowed for an efficient and consistent flag definition.

3.1. Prior Probability

The chosen prior formulation is based on the SST. As the ECMWF forecast SST field is available in SWIM products, a simple prior can be derived based on a pseudo melting criterion, at temperature T set to 276 K. Allowing for an arbitrary standard deviation of $\Delta T = 1$ K for the ECMWF SST, and assuming Gaussian statistics, the a priori probability of sea-ice presence writes:

$$p(\text{ice}) = \frac{1}{2}\int_{-\infty}^{T} \frac{dT'}{\sqrt{2\pi}\Delta T} \exp\left[-\left(\frac{\text{SST} - T'}{\sqrt{2}\Delta T}\right)^2\right]. \tag{9}$$

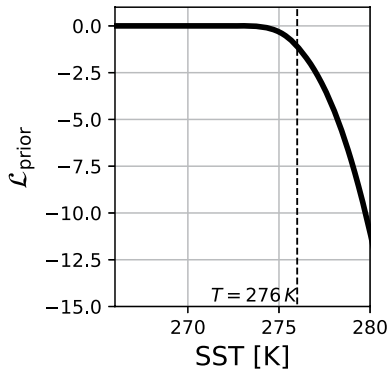

Figure 3. Prior log-likelihood, with $T = 276$ K and $\Delta T = 1$ K (see Equations 8 and 10).

The 1/2 factor constrains the prior between 0 (no ice) and 1/2 (ice and open water equiprobability). Equation 9 can be expressed with the error function

$$p(\text{ice}) = \frac{1}{4}\left[1 + \text{erf}\left(\frac{276\,\text{K} - \text{SST}}{\sqrt{2}\Delta T}\right)\right]. \tag{10}$$

For consistency, the prior probability of open water is defined as the complementary of the sea-ice probability:

$$p(\text{water}) = 1 - p(\text{ice}). \tag{11}$$

The corresponding prior log-likelihood is plotted in Figure 3 from Equation 8. This a priori does not favor the detection of sea-ice but only penalizes it at low latitudes, where the SST exceeds 276 K, thus preventing spurious sea-ice detections.

3.2. Practical Log-Likelihood Estimate

3.2.1. Statistical Model

A log-normal distribution is assumed for the NRCS likelihood:

$$p(\sigma|\text{x}) = \frac{\lambda}{\sigma\sqrt{2\pi}\Delta\sigma_\text{x}}\exp\left\{-\left[\frac{\text{dB}(\sigma) - \mu_\text{x}\ )}{\sqrt{2}\Delta\sigma_\text{x}}\right]^2\right\}, \tag{12}$$

where

$$\text{dB}(\sigma) = 10\log_{10}(\sigma) = \lambda \ln\sigma, \tag{13}$$

and $\lambda = 10/\ln 10 \simeq 4.3$. Although the log-normal distribution is a crude simplification of the empirical distributions, it seems to be a convenient choice in our case, with a good compromise between suitability and complexity. First, a normal distribution cannot be chosen, as NRCS values are defined only over positive reals. This assumption breaks down when looking at NRCS distributions in dB, which is the reason why a log-normal assumption seems reasonable. Moreover, the log-normal assumption is quite convenient in our case as it is based on only two parameters, μ_x and $\Delta\sigma_\text{x}$ which relate directly to NRCS mean and standard deviation.

Hence, the log-likelihood (Equation 7) writes:

$$\mathcal{L} = \left[\frac{\text{dB}(\sigma) - \mu_\text{water}}{\sqrt{2}\Delta\sigma_\text{water}}\right]^2 - \left[\frac{\text{dB}(\sigma) - \mu_\text{ice}}{\sqrt{2}\Delta\sigma_\text{ice}}\right]^2 + \ln\left(\frac{\Delta\sigma_\text{water}}{\Delta\sigma_\text{ice}}\right) + \mathcal{L}_\text{prior}. \tag{14}$$

3.2.2. Parameters Estimation From Data

Parameters appearing in the log-likelihood, Equation 14 are evaluated from ancillary meteorological data available in SWIM products. Their behavior must be constrained from past observations, under the so-called GMFs. They are estimated from NRCS average mini profiles (L2 products) in linear units:

$$\sigma_\text{x} = \text{E}(\sigma|\text{x}), \tag{15}$$

where E is the expectation, estimated itself by ensemble average. Their empirical estimation and parameterization are detailed in Section 3.4.

From now on, parameters Δ_x and μ_x can be estimated using the method of moments. First, the standard deviation in dB is:

$$\Delta\sigma_x = \lambda\sqrt{\ln\left[1 + \frac{\mathrm{Var}\,(\sigma|\mathrm{x})}{\mathrm{E}(\sigma|\mathrm{x})^2}\right]}, \tag{16}$$

with the mean $\mathrm{E}\,(\sigma|\mathrm{x})$ and variance $\mathrm{Var}\,(\sigma|\mathrm{x})$ being estimated from the L2 miniprofiles averages and standard deviation. This shortcut is acceptable as long as both mean and variance variability within each 0.5° miniprofile incidence bin can be neglected, which is assumed here. Second, the μ_x parameter, which does not only depend on the GMF, is expressed in dB as:

$$\mu_x = \mathrm{dB}(\sigma_x) - \Delta\sigma_x^2/(2\lambda). \tag{17}$$

3.3. Maximum Likelihood Combination of Neighboring Flag Estimates

For both visualization and application purposes, it is useful to have an optimal mean of combining neighboring estimates of the L1a flag. Indeed, a profile as provided by the L1 product is composed of no less than a few hundreds or thousands of NRCS measurements. For the present case, they are hard to plot on a single figure, and the comparison with lower resolution external references may not be adequate. Assuming homogeneity of the surface for N neighboring SWIM measurements (for example the N points of a profile), a maximum likelihood estimator of the combined flag is defined similarly to Equation 5

$$P_{\{1\ldots,N\}}(\mathrm{ice}) = \frac{p(\mathrm{ice}|\sigma_1,\ldots,\sigma_N)}{p(\mathrm{ice}|\sigma_1,\ldots,\sigma_N) + p(\mathrm{water}|\sigma_1,\ldots,\sigma_N)}. \tag{18}$$

Assuming the σ_j to be i.i.d. random variables,

$$p(\mathrm{x}|\sigma_1,\ldots,\sigma_N) = \prod_{j=1}^{N} p(\mathrm{x}|\sigma_j). \tag{19}$$

Then, Equation 18 can be rewritten as:

$$P_{\{1\ldots,N\}}(\mathrm{ice}) = \frac{1}{1 + e^{-\mathcal{L}_{\{1\ldots,N\}}}}, \tag{20}$$

where

$$\mathcal{L}_{\{1\ldots,N\}} = \sum_{j=1}^{N} \mathcal{L}_j, \tag{21}$$

and

$$\mathcal{L}_j = \ln\left[\frac{p(\mathrm{ice}|\sigma_j)}{p(\mathrm{water}|\sigma_j)}\right] \tag{22}$$

is the log-likelihood of measurement j. The sea-ice flag for the set {1, …, N} is then

$$\mathrm{flag}_{\{1\ldots,N\}} = H(\mathcal{L}_{\{1\ldots,N\}}). \tag{23}$$

In practise, the mean log-likelihood is preferred, as it should only weakly depend on N:

$$\mathrm{flag}_{\{1\ldots,N\}} = H(\bar{\mathcal{L}}_{\{1\ldots,N\}}), \tag{24}$$

with

$$\bar{\mathcal{L}}_{\{1\ldots,N\}} = \frac{1}{N}\mathcal{L}_{\{1\ldots,N\}}. \tag{25}$$

As a consequence, assuming homogeneity of the scene for a set of NRCS measurements, an optimal flag estimator (in the sense of maximum likelihood estimators) is obtained by averaging the individual log-likelihoods. Since the averaging operation is linear, one can even consider higher-level combinations, for example, combinations

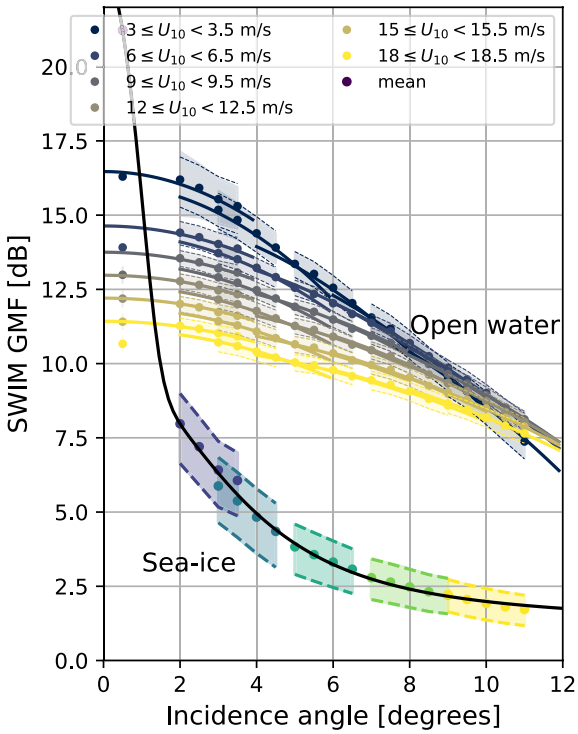

Figure 4. Distribution of Normalized Radar Cross-Section over open water and sea-ice as a function of incidence angle for each SWIM off-nadir beam. The nadir beam averages are plotted at 0.5° incidence. For the open water case, the GMF is further detailed by wind speed. The dots are GMF estimates from data using Equation 15. Their least squares fit for open water and for sea-ice is plotted in solid lines. The colored sector around the GMF corresponds to the $\pm 0.5\Delta\sigma_x$ interval. Its least squares fit is plotted in thin dashed lines.

between beams with different incidences, without having to know the detail of all the individual measurements log-likelihoods.

3.4. Geophysical Model Functions

In the present algorithm, GMFs constrain flag estimates based on prior empirical distributions that are assumed to be stable along time. For this reason, the data base used for their estimation must be representative of the flag usage: it will be used all along the year and over both the northern and southern hemispheres. This data base is composed of all miniprofiles at latitudes above 50°N and below 50°S from March 1, 2020 to March 1, 2021. The hypothesis open water or sea-ice is derived from the auxiliary meteorological files sea-ice concentration (SIC). The open water case corresponds to SIC = 0 while sea-ice is assumed when SIC > 0.9. In both cases, the land-sea mask is checked to be 0 (ocean).

3.4.1. Open Water GMF

SWIM open water GMF is plotted as a function of wind speed and incidence angle in Figure 4, from Equations 15 and 16.

Part of the observed NRCS distribution deviation can be explained by an additional sea-state dependence. Sea-state is usually measured by the significant wave height H_S, conventionally defined as 4 times the standard deviation of the elevations. A mean H_S related NRCS deviation can be defined by

$$\delta = \mathrm{dB}\left[\mathrm{E}(\sigma|U_{10}, H_S)\right] - \mathrm{dB}\left[\mathrm{E}(\sigma|U_{10})\right]. \tag{26}$$

and plotted in Figure 5. The sea-state dependence increases with decreasing wind speed. Its relative contribution reaches up to 3 dB at low wind speeds and becomes negligible toward larger winds. Although not shown here, attempts to derive a physics-based NRCS parameterization as a function of H_S proved usefulness at low wind speeds, but introduced an artificial bias at larger ones due to fitting errors. Consequently, the GMF explicit dependence on H_S is dropped in this study. This effect however appears in the residual GMF standard deviation (Equation 16).

Following the Geometric Optics formulation (Boisot et al., 2015; Nouguier et al., 2016), the near-nadir NRCS dependence with incidence angle over open water is known to follow:

$$\sigma_W = \frac{|R|^2}{\cos^4\theta \mathrm{mss}_{\mathrm{eff}}} \exp\left(-\frac{\tan^2\theta}{\mathrm{mss}_{\mathrm{eff}}}\right) \tag{27}$$

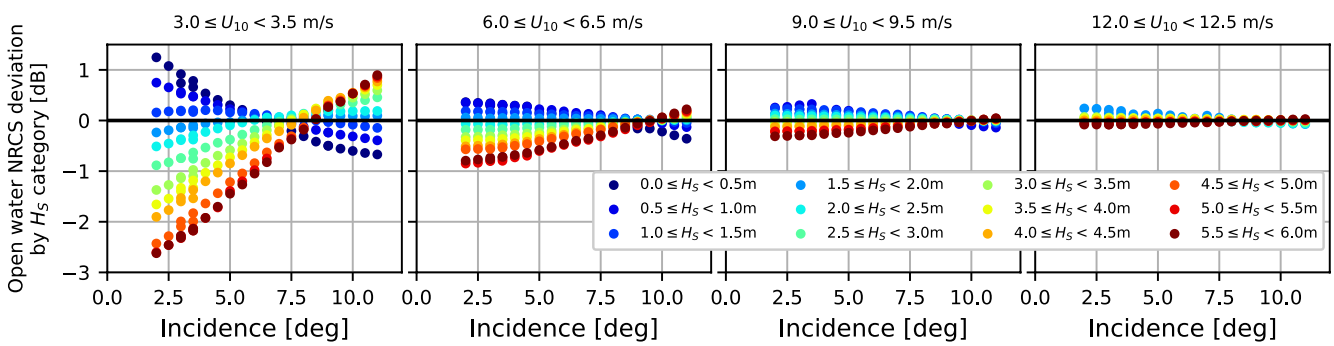

Figure 5. Distribution of Normalized Radar Cross-Section (NRCS) deviation from Equation 26 by H_S category over open water as a function of incidence angle for all off-nadir beams for four different wind speeds.

Table 2
Table of Coefficients for $|R|^2$ (Equation 28)

i	1 (2°)	2 (4°)	3 (6°)	4 (8°)	5 (10°)
$\|R\|_i^2$	0.64	0.54	0.66	0.69	0.70
ρ_i	0.44	0.27	0.44	0.55	0.69
λ_i [(m/s)$^{-1}$]	0.47	0.47	0.44	0.50	0.47
s_i [(m/s)$^{-1}$]	0.013	0.010	0.0070	0.0083	0.0071

More sophisticated models (Boisot et al., 2015; Chapron et al., 2000; Nouguier et al., 2016) can be considered, but which only bring improvements at higher incidences and/or lower radar frequency. Nouguier et al. (2016) used the same kind of parameterization for their analysis of GPM data in Ku band. Here, $|R|^2$ is to be interpreted as a Fresnel reflection coefficient, which by definition should be positive and lower than 1. The mss_{eff} parameter can be interpreted as a filtered version of the Mean Square Slope (mss) derived from ocean waves spectra (Boisot et al., 2015).

Over open water, the GMF is assumed to depend on U_{10}, the incidence angle θ and the beam number. $|R|^2$, mss_{eff} and $\Delta\sigma_{\text{water}}$ (Equation 16) are empirically parameterized as a function of wind speed and beam number i = 1, …, 5, with central incidences $\theta_i = 2i$ degrees, inspired by preliminary works on GPM (Yan et al., 2019):

$$|R|^2 = |R|_i^2 / \left(1 + \rho_i e^{-\lambda_i U_{10}}\right) - s_i U_{10}, \tag{28}$$

$$\text{mss}_{\text{eff}} = M_i / \left(1 + \nu_i e^{-\xi_i U_{10}}\right) + t_i U_{10}, \tag{29}$$

$$\Delta\sigma_{\text{water}} = \Delta\Sigma_i + \alpha_i e^{-\beta_i U_{10}^2} + \upsilon_i U_{10}. \tag{30}$$

Least squares fitting coefficients appearing in Equations 28–30 are summarized in Tables 2–4, and plotted in Figures 6–8. The GMF dependence over azimuth angle relative to the wind direction is not investigated here.

To our knowledge, it is the first time that near-nadir NRCS profiles are estimated at various incidences independently. In the past, studies had been lead on Ku-band near-nadir scatterometers such as TRMM (Freilich & Vanhoff, 2003) or GPM (Nouguier et al., 2016). In both studies, incidences span the whole range from 0° to 18°. Effective mss estimates from these studies are in agreement with ours (Figure 7), especially with the 6° beam. This evolution of the effective mss with the nominal incidence is also expected due to diffraction/curvature effects (see Appendix A and Equation A9). Also, the fact that the mss does not fall to 0 at 0 m/s wind speed can be understood through the effect of the remaining surface waves, which is more important at low wind speeds (see Figure 5). As far as the reflection coefficient is concerned, only Freilich and Vanhoff (2003) and Chen et al. (2018) provided such estimate from TRMM data. The agreement with our figure is satisfying for the sea-ice flagging, especially again with the 6° beam. Diffraction/curvature effects predict a slight increase of the fitted reflection coefficient (see Appendix A, Equation A10), on top of which inter-beam biases may come into play to explain the results of Figure 6. Especially, a positive interbeam bias is visible in Figure 4 on the 2° beam, that can explain the nonuniform evolution of the reflection coefficient with incidence in Figure 6. A NRCS overestimation by the 2° is also observed by Hauser et al. (2021) (their Figure 10a) and Ren et al. (2021) (their Table 2). Finally, the standard deviation $\Delta\sigma$ is here presented for the first time over open water. The increase of spread at low wind speeds corroborates the higher sea-state dependence observed in Figure 5. Then, the spread is essentially independent of incidence over open water, except for the 2° beam at low wind speeds.

3.4.2. Sea-Ice GMF

The sea-ice backscatter is commonly modeled as the sum of a surface scattering and a volume scattering terms (Remund & Long, 2003). Over sea-ice, exponential correlation is often assumed, which leads to a surface scattering of the type (Hagfors, 1970; Kurtz et al., 2014):

$$\sigma_{\text{surf}} \propto \left(1 + \gamma \sin^2\theta\right)^{-3/2}, \tag{31}$$

Table 3
Table of Coefficients for mss_{eff} (Equation 29)

i	1 (2°)	2 (4°)	3 (6°)	4 (8°)	5 (10°)
M_i	0.015	0.014	0.014	0.037	0.033
ν_i	5.3	2.3	0.42	1.19	0.60
ξ_i [(m/s)$^{-1}$]	0.72	0.52	0.39	0.070	0.0
t_i [(m/s)$^{-1}$]	0.00074	0.00075	0.0017	0.0021	0.0015

where γ (constant) can be interpreted as an angular scattering efficiency. The volume scattering term is (Remund & Long, 2003):

$$\sigma_{\text{vol}} \propto \cos\theta, \tag{32}$$

which is essentially constant at near-nadir incidences. The combination of a surface scattering (Equation 31) with a volume scattering term (Equation 32) is fitted over off-nadir average miniprofiles of Figure 4. In addition, a nadir correction is inspired from Giles et al. (2007):

Table 4
Table of Coefficients for $\Delta\sigma$ in dB Over Open Water (Equation 30)

i	1 (2°)	2 (4°)	3 (6°)	4 (8°)	5 (10°)
$\Delta\Sigma_i$ [dB]	0.46	0.50	0.46	0.47	0.47
α_i [dB]	1.8	1.1	0.95	1.15	1.15
β_i [(m/s)$^{-2}$]	0.049	0.059	0.10	0.10	0.078
v_i [dB/(m/s)]	0.0038	0.0054	0.0042	0.0084	0.0081

$$\sigma_{\text{nadir}} \propto e^{-(\theta/\theta_{\text{pr}})^2}, \tag{33}$$

which is fitted over the whole range of incidences, including nadir. Finally, the full sea-ice GMF reads:

$$\sigma_I = A\left(1+\gamma\sin^2\theta\right)^{-3/2} + B\cos\theta + Ce^{-(\theta/\theta_{\text{pr}})^2}, \tag{34}$$

with variables numerical values obtained from the fitting procedure gathered in Table 5. It is plotted in Figure 4. Although these coefficients are derived from physical parameterizations, it does not seem possible to interpret them in terms of the physical properties of the sea-ice: the data on which the GMF was estimated includes multiple types of sea-ice (e.g., FYI, MYI), and this effective GMF implicitly incorporates their statistical distribution in the training database. Similarly to the open water case, an empirical parameterization is found for the sea-ice standard deviation in dB:

$$\Delta\sigma_{\text{ice}} = a_i\tan^2\theta + b_i. \tag{35}$$

Least squares fitting coefficients a_i and b_i are gathered in Table 6 and the resulting parameterization plotted in Figure 9.

3.5. Test Case: Weddell Sea

A test case is selected over an open water sea-ice transition in the marginal ice zone offshore of the eastern Weddell Sea on October 7, 2020, when the sea-ice extent is usually maximum around Antarctica (see Figure 10a). CFOSAT sampled this region around 07:30 UTC while Sentinel-1 flew over it approximately 13 hr later. The HV channel NRCS of Sentinel-1 (Figure 10b) is used as a qualitative ground-truth illustration for the situation at that time, which enables direct visualization of the scene measured by SWIM. Especially, from this SAR image, sea-ice appears very variable at that location, with the presence of heterogeneous sea-ice mesoscale features and melting sea-ice.

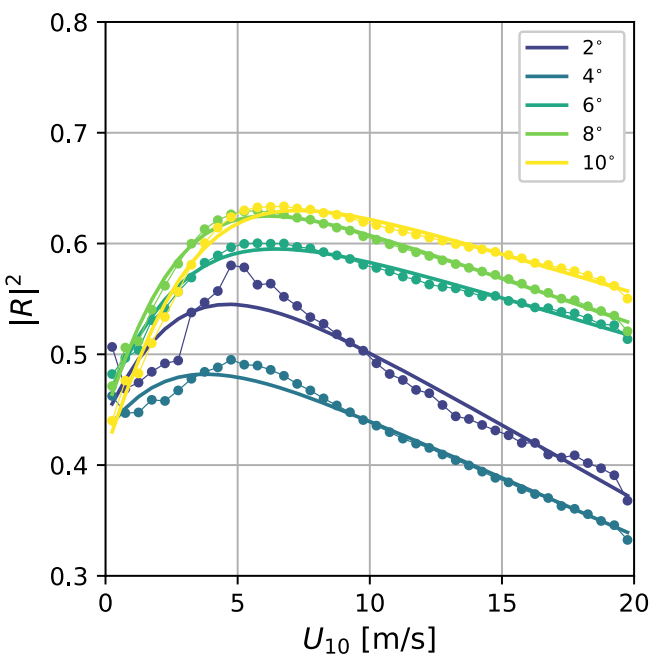

Figure 6. $|R|^2$ parameter estimated from least squares fitting of average Normalized Radar Cross-Section profiles (Equation 15) (dots) and parameterization (Equation 28) (solid line) for SWIM off-nadir beams.

First, the presence of open water and sea-ice on both sides of the margin are correctly identified, according to the sign of the beam level log-likelihood (Figure 10g). Its color (blue or red) corroborates the observed similarity between each of the GMFs (Figures 10e and 10f) and the NRCS (averaged over profiles). The SWIM L1 NRCS profile corresponding to beam 10° (see red square in Figures 10d–10g) is analyzed across an open water/sea-ice transition (detected by the SAR data) in Figure 10c. Between 9° and 9.8° incidence, the profile is quite stable and close to the open water GMF. Consistently, the estimated probability of sea-ice presence is constantly equal to 0, indicating an open water area. The transition to sea-ice occurs in two steps: after a sharp decrease of the NRCS (black curve) around 10° incidence, the NRCS undergoes a second decrease after 10.7° incidence with a steepest slope. The algorithm should flag these two areas as sea-ice, with slightly lower probability over the 10–10.7° interval.

4. Flag Qualification

In the absence of fully reliable ground truth simultaneously colocated with SWIM, the qualification of the proposed flag against other sea-ice data must be carried out with a critical eye. Here, sea-ice flag references are derived from sea-ice concentration maps. As there is no consensual sea-ice concentration threshold for this flagging, this variability is also explored in what follows. A first reference is the one embedded in SWIM NRT products, i.e., ECMWF ice concentrations. A second reference is the SSMI sea-ice concentration products processed at Ifremer (see Section 2.2).

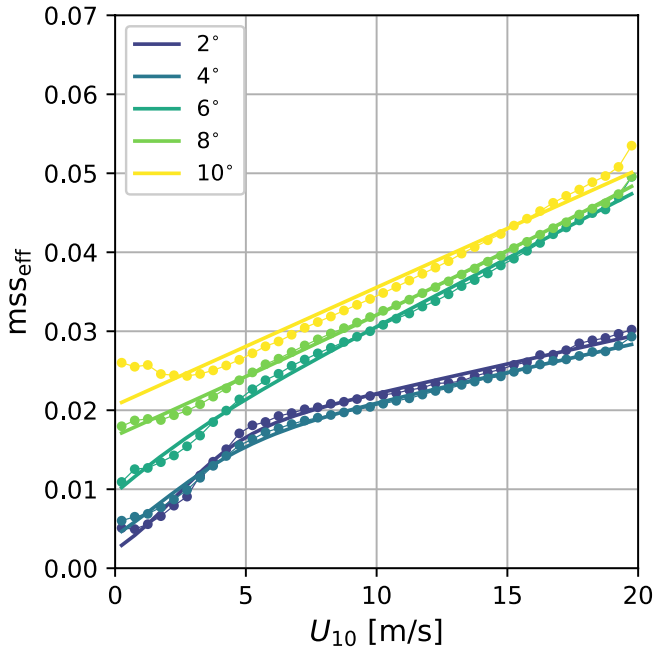

Figure 7. mss_{eff} parameter estimated from least squares fitting of average Normalized Radar Cross-Section profiles (Equation 15) (dots) and parameterization (Equation 29) (solid line) for SWIM off-nadir beams.

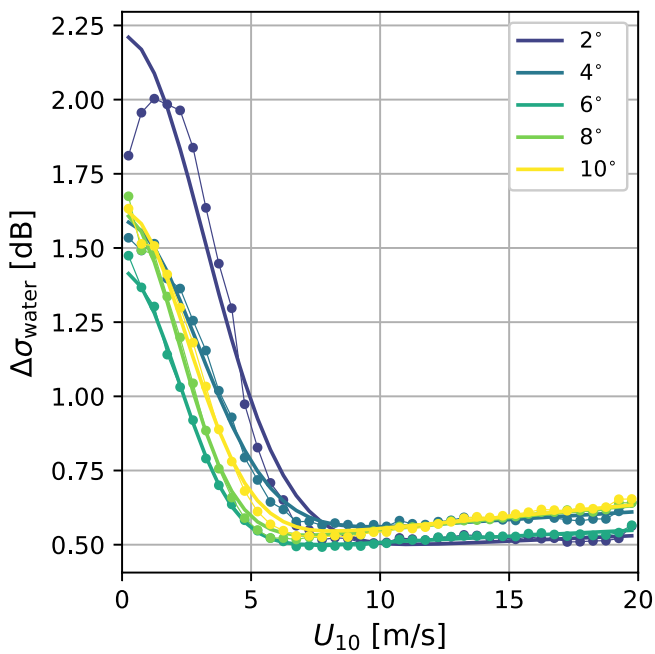

Figure 8. Standard deviation over open water in dB estimated from least squares fitting of average Normalized Radar Cross-Section profiles (Equation 15) (dots) and parameterization (Equation 30) (solid line) for SWIM off-nadir beams.

Sea-ice is flagged in SWIM L1a profiles for the period between January 15 and 28, 2021 included, this period corresponding to SWIM cycle 63 at latitudes above 40°N and below 40°S. It is interesting noticing that the data used for the GMF derivation in Section 3.4 are taken from the L2 products, while they are here taken from L1a products. The latitudes are limited in order to focus on sea-ice covered regions. The latitude limit is lowered to 40°N in order to include the Caspian and Black Sea which undergo a sea water freezing episode at that time of the year. Nevertheless, the sea-ice flag design, through the inclusion of a latitude dependent a priori prevents any spurious sea-ice detection at low latitudes. L1 flags are combined according to the method in Section 3.3 before being compared to references. References are colocated with SWIM profiles using a nearest neighbor algorithm. In January, situations are quite contrasted between the poles: Arctic is characterized by intense sea-ice formation while the melting is already quite advanced around Antarctica. Thus, sea-ice types differ, with quite young and dry ice in the Arctic marginal ice, and older wet sea-ice around Antarctic.

A convenient way of qualifying a classification against a ground-truth data set is the confusion matrices formalism. For a given sea-ice threshold, a confusion matrix provides an inventory of the profiles according to their labels with respect to SWIM on the one hand and the reference data set on the other hand. An example of such a matrix is provided in Table 7 for the 8° beam. Sea-ice detections are qualified of positive: these are either True Positives (TP) when sea-ice is detected by both methods, and False Positives (FP) when sea-ice is only detected by SWIM. Cases when no sea-ice is present are referred as negatives: True Negatives (TN) when both methods are in agreement, and False Negatives when sea-ice is detected by the reference but not by SWIM. If the reference and SWIM agree perfectly, only the matrix diagonal elements are non-zero. Looking at confusion matrix in Table 7, the largest populations are found along diagonal elements. According to SSMI with a threshold at 0.5 sea-ice concentration, 15.97% of the echoes above 40° latitude are classified as sea-ice, against 15.84% for SWIM. The false negative rate is the percentage of spurious open water detections by SWIM when considering the ground truth as reference:

$$\mathrm{FNR} = \frac{\mathrm{FN}}{\mathrm{TP} + \mathrm{FN}}. \tag{36}$$

In the present case, this situation occurs for 7.49% of the macrocycles over sea-ice. The false negative rate is an analog to the false positive rate when considering open water instead of sea-ice:

$$\mathrm{FPR} = \frac{\mathrm{FP}}{\mathrm{FP} + \mathrm{TN}}. \tag{37}$$

Here, 1.27% of the open water macrocycles are mistakenly labeled as sea-ice considering SSMI as reference. Although these rates are quite meaningful, neither of them combines all the confusion matrix elements into a single number. Among others, the accuracy metrics seems adapted:

$$\mathrm{ACC} = \frac{\mathrm{TP} + \mathrm{TN}}{\mathrm{TP} + \mathrm{TN} + \mathrm{FP} + \mathrm{FN}} \tag{38}$$

which quantifies the rate of agreement between classifications. The accuracy can be thought as an optimal indicator of the agreement between two classifications: a 100% accuracy corresponds to a perfect agreement between both data sets, and hence to zero off-diagonal elements. Here, it reaches 97.73%. At that level, the remaining 2.27% of data points where SWIM and SSMI

Table 5
Table of Coefficients for SWIM GMF Over Sea-Ice, Equation 34

A	γ	B	C	θ_{pr} (°)
8.7	401	1.4	202	0.7

disagree is hard to distinguish with separate figures. It can be concluded from a first look at classification results that both SWIM and SSMI are in excellent agreement overall.

Although the previous example is quite representative of SWIM sea-ice flag performances, it is interesting to look in details at the sensitivity of the previous metrics, defined in Equations 36–38, to the sea-ice concentration threshold, beam by beam, and for both reference data sets, as it is presented in Figures 11 and 12. Overall, performances are similar from beam to beam. Looking at the accuracy, it is worth noting that the accuracy of SWIM sea-ice flag is greater with SSMI than with the ECMWF derived flag (currently in SWIM product), thus confirming the added value of such a flag compared to the current one. Now looking at disagreements between data set in Figure 11, it is interesting looking at their sensitivity to sea-ice concentration. Looking at the FNR slope, it can be seen that the sensitivity to the presence of water among sea-ice is decreased with increasing beam nominal incidence: the 10° beam is more inclined to detect low sea-ice concentration areas than is the 2° beam. On the other hand, the false positive rate slightly increases with incidence: the 10° beam could also be more inclined to spurious sea-ice detections.

Back to Figure 12, it is interesting to look at the SIC threshold for which the accuracy is maximum (vertical solid and dashed lines). This information is summarized in Table 8. First, as was already observed previously, the overall agreement between SWIM and SSMI is better than with SWIM and ECMWF forecast: accuracies are all greater in the first case. Second, the SIC threshold of best agreement decreases with the beam incidence angle. This corroborates the already observed increased sensitivity of beams with incidence. Second, the optimum SIC threshold goes down to 0.10 for the 10° beam. It must be noticed that the sea-ice category was defined during the GMF conception with a threshold of 0.9 on the colocated sea-ice concentration (see Section 3.4), thus not guarantying intermediate concentrations to be properly accounted for.

At that stage, validity limits of the reference data sets are probably reached. The disagreement between SWIM and the references could not only be caused by spurious detections. SWIM profile level flag results are compared to a flag built from SSMI data with a concentration threshold set at 1%, both at the North (Figure 14) and South poles (Figure 15). A first visual inspection informs that most of the sea-ice pack is indeed detected as such on all beams (blue dots), both in Arctic and Antarctic. Another look at the data shows the relatively low number of spurious detections at low latitudes (confirmed by a global map of flagged data), thanks to the definition of the prior and the application of the land-sea mask.

False negatives (sea-ice areas missed by SWIM) are colored according to their sea-ice concentration in the SSMI product. Most of them correspond to low ice concentrations (purple patches), but some locations with higher concentration are missed. These are located either along the coastlines or occasionally inside the ice pack for low incidence beams. False negatives close to the coastlines can be attributed to the presence of ice shelves near the continents, which radar signature may be further from the one of sea-ice than from the one of open water. For the second kind, this can be explained by the presence of melting sea-ice in the South pole. Indeed, at that time of the year, the sea-ice extent in the Arctic is still growing, while it is almost at its minimum in the Antarctic. Thus, sea-ice types differ in Figures 14 and 15, with a tendency to freezing in the North and to melting in the South. Melting sea-ice, as it mixes with water, may have a less distinct signature from the one of open water.

Looking now at spurious sea-ice detections (golden triangles), two main observations can be drawn. First, most of these detections occur in the marginal ice zone (close to Svalbard in the North), where low sea-ice concentrations are likely to occur. Second, the number of these detections increases with the beam nominal incidence. The case of the Amundsen Sea and Ross Sea (90°–180°W) is particularly instructive. As the number of false positives increases, the number of false negatives decreases as well, especially for the 8° and 10° beams, meaning that these false positives, may not be all spurious and may contain some signal, which is complementary to SSMI. Finally, coherent structures (present on 6° to 10° beams) appear offshore of Antarctica, which, at that time of the year, could correspond to icebergs.

Table 6
Table of Coefficients for $\Delta\sigma$ in dB Over Sea-Ice, Equation 35

i	1 (2°)	2 (4°)	3 (6°)	4 (8°)	5 (10°)
a_i (dB)	−70	−9.8	−31	−16	−4.7
b_i (dB)	2.2	2.0	1.8	1.6	1.2

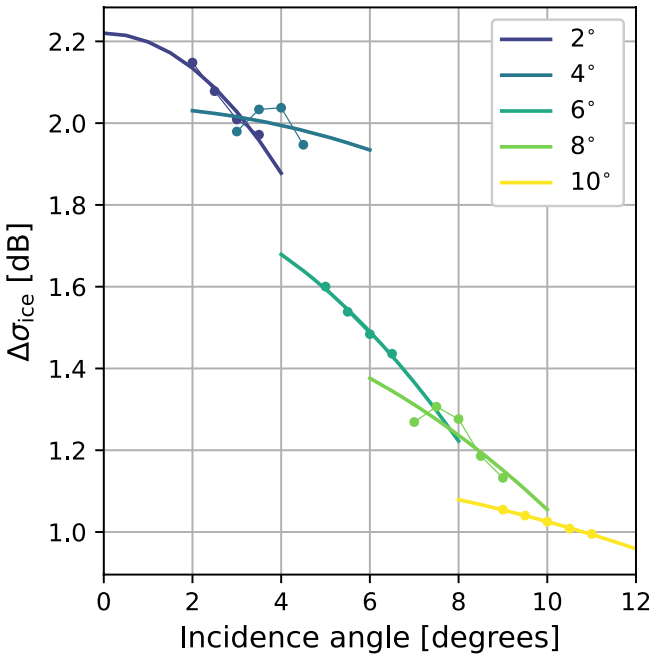

Figure 9. Standard deviation over sea-ice in dB estimated from least squares fitting of average Normalized Radar Cross-Section profiles (Equation 15) (dots) and parameterization (Equation 35) (solid line) for SWIM off-nadir beams.

It is worth noting that there is an increased sensitivity to sea-ice with beam incidence. Two main reasons could probably be at its roots. First, the sensitivity to sea-ice detection decreases with incidence (above 2°), as can be seen in Figure 13. The average NRCS ratio in dB

$$\mu = \mu_{\text{ice}} - \mu_{\text{water}}, \tag{39}$$

is plotted in Figure 13 at various wind speeds. On the other hand, the sea-ice response gets closer and closer to the noise level with increased central incidence. Two effects must be considered. The figure shows the first one, namely the theoretical separability of the open water/sea-ice echoes. We can take the comparison of the 4° and 10° beams as an example. At 10°, μ is lower than at 4°. For this reason, the open water/sea-ice transition will be more pronounced at 4° than at 10°, thus limiting the number of false detections at 4°. The analysis in Figure 13 does not take into account the noise level of each beam. Again, it can be argued that the detection quality is better at 4° than at 10° because of the higher signal-to-noise ratio at low incidence. However, this analysis can be weighted by observing that the wind dependence of μ is more important at low incidence, which suggests different performances with different wind speeds. Further studies need to be conducted in order to better characterize it.

5. Conclusion

A Bayesian approach is proposed to discriminate sea-ice from open water in near-nadir microwave NRCS observations. It is specifically designed for Ku-Band SWIM/CFOSAT data sets, but intrinsically, the method is more general. The main principle is to compare in a statistical sense the measured values of NRCS to GMFs which relate the NRCS to wind speed and incidence angle. First the GMF models have been established. Then, the inversion method has been applied to SWIM data. The comparison of its results with model and remote sensing-based reference data sets exhibits performances that reach up to 98% accuracy. A prior probability based on SST is defined that prevents any spurious sea-ice detection at low latitudes, i.e., where the SST exceeds 276 K. Moreover, this new lag performs better than the existing flag, as it compares more satisfyingly with external remote sensing-based data. More quantitatively, at polar latitudes, the present flag is in disagreement with reference data in less than 4% of the time, and without any combination of beam incidences. Sensitivity increases with incidence, and the intermediate incidence beams (4° and 6°) exhibit the highest agreement with reference data sets.

Yet, performances assessment provides interesting insights into the scientific content of SWIM data for sea-ice studies. In addition, there are evidences that SWIM may be able to identify more particular features such as icebergs or particular sea-ice types, that may not be detected by radiometers such as SSMI. Especially, the larger incidence beams (8° and 10°) detect features away from the marginal ice zone that are consistent from a beam to another. In addition, GMFs are derived that can be used for the improvement of SWIM data processing. Also, one could think of properly diagnosing the flag performances seasonality by looking at a whole year of such processing.

Perspectives opened by this study are vast and would benefit of additional validation efforts. At the moment, comparisons have been carried out at the profile level with typically 10 km resolution reference data. The present flag being defined at very high resolution (see Table 1), high resolution ground truths are needed. One can think of optical or SAR images for example, The exact nature of false positive detections at large incidences could be qualified using iceberg data bases (Tournadre et al., 2008).

This algorithm is a base-line algorithm that could be improved. For example, the dependence of the standard deviations on sea-state could be taken into account. Sea-ice GMF could be refined by a proper accounting of sea-ice types (age, thickness, wetness,

Table 7
Confusion Matrix for the 8° Beam Profile Level Flag 24 Compared to SSMI Forecast With 0.5 Concentration Threshold for Latitudes Above 40°N and Below 40°S for SWIM Cycle 63

SSMI flag \ SWIM flag	0	1
0 (no sea-ice)	TN = 2309896	FP = 29802
1 (sea-ice)	FN = 33329	TP = 411407

Note. The number of data points entering in each category is represented in the table.

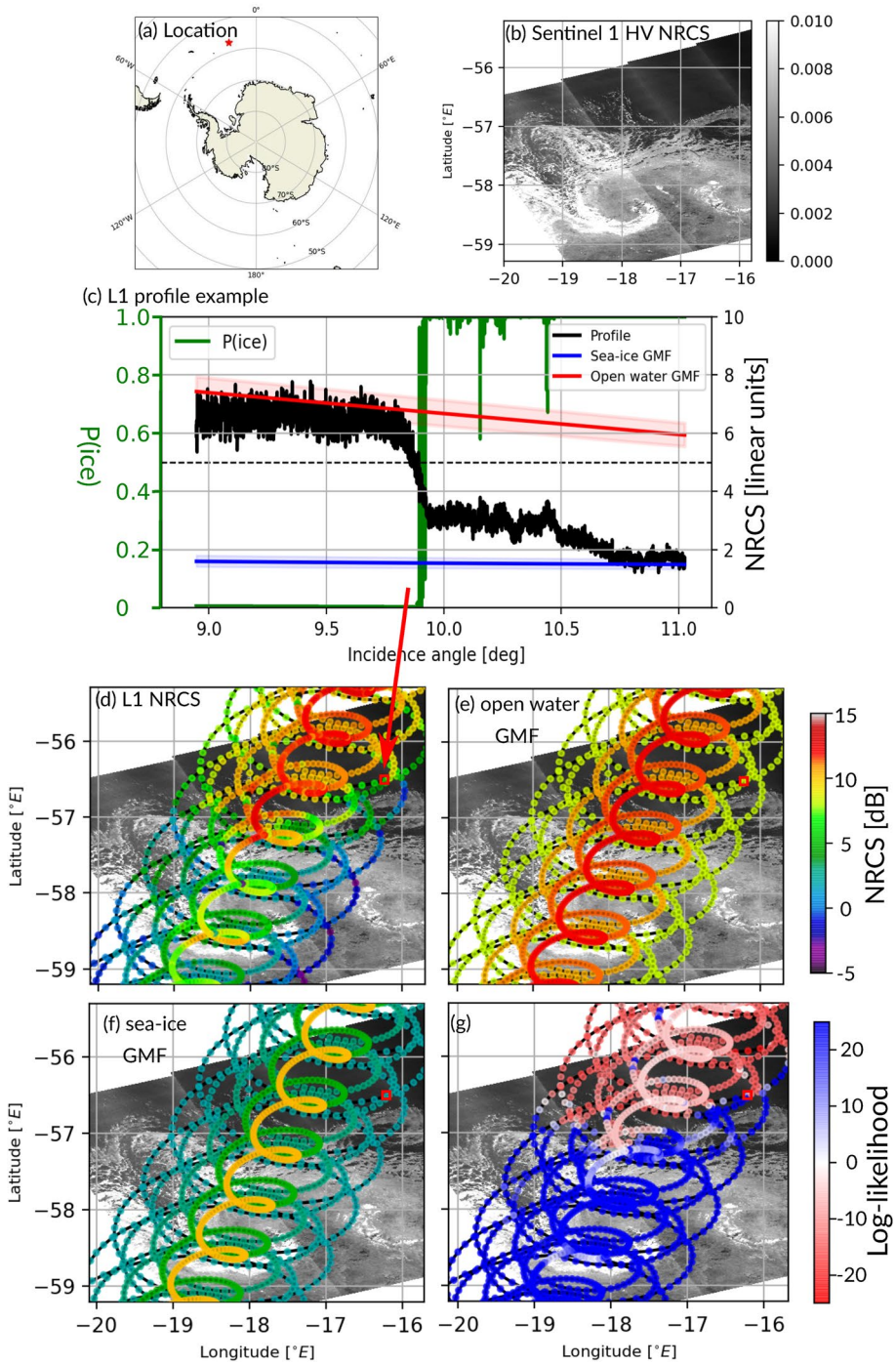

Figure 10. Test case at an open water/sea-ice transition. (a) Location of the center of the scene (red star). (b) Sentinel-1 Normalized Radar Cross-Section (NRCS) in HV polarization. (c) L1 NRCS profile example. The raw NRCS profile is plotted in black (with y axis labels on the right), together with the open water (red) and sea-ice Geophysical Model Functions (GMF, blue), with their standard deviations underlayed (light blue and light red). The sea-ice probability is plotted in green (y axis labels on the left). The dashed line, represents the limit $P(\text{ice}) = 0.5$. At that geographical location $U_{10} = 4.7$ m/s and $H_S = 2.5$ m. The red arrow links the subfigure (c) with the subfigure (d) to show which position is plotted. (d) L1 NRCS averaged over each profile (1 value per azimuth position of a beam). The colors show clearly two classes (ice/no ice) matching the boundaries of the S1 images. (e) Open water GMF averaged over each profile (1 value per azimuth position of a beam). (f) same as (e) for sea-ice (1 value per azimuth position of a beam). (g) Profile level log-likelihood (Equation 25).

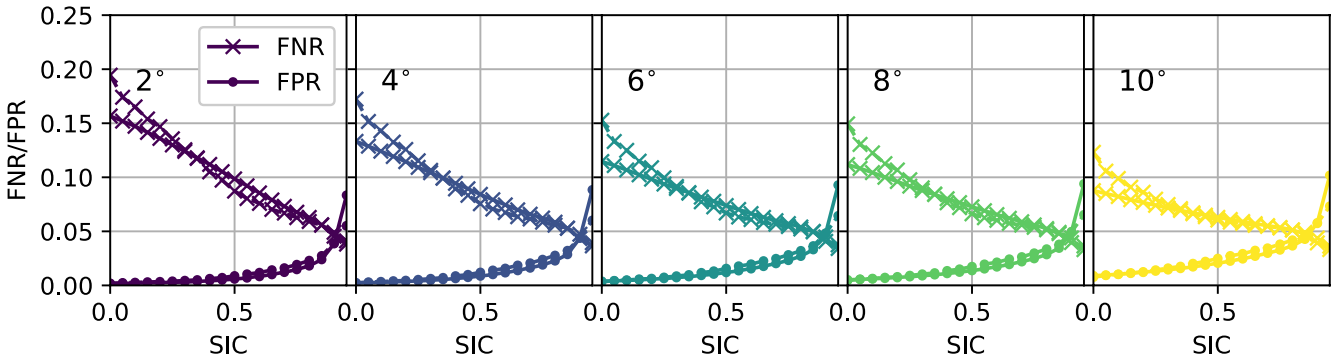

Figure 11. Probability of disagreement between SWIM and ECMWF classification (dashed lines) or SSMI sea-ice (solid lines) reference data sets for latitudes above 40°N and below 40°S. These disagreements can be decomposed into False Negatives (crosses, decreasing with sea-ice concentration (SIC)), Equation 36, and into False Positives (dots, increasing with SIC), Equation 37.

etc.), and thus its uncertainty diminished. More specifically, the distinction between FYI and MYI would be a first way to account for all these effects. Spatiotemporal dependencies of the GMF can be considered, for example, on the hemisphere or seasonal variation. Similarly the azimuthal dependence of the open water GMF is known to exist and could be taken into account. It could also be adapted to GPM Dual Polarization Radar data in the same radar band and at similar incidence angles (Hauser & Tison, 2018).

Based on this study, the definition of sea-ice products from SWIM observations is in progress. Combining incidences seems an interesting way to further characterize sea-ice, that builds up on SWIM acquisition geometry. In a second step, the scatterometer on board CFOSAT could be used in fusion with SWIM, and next generation satellite missions operating near nadir, such as SWOT, could benefit from this work.

Appendix A: Curvature Effect With Incidence on Effective Parameters $\mathrm{mss}_{\mathrm{eff}}$ and $|R|^2$ Over Open Water

For the present study, Geometrical Optics model (Equation 27) is assumed. However, this does not account for curvature and diffraction related effects (Guimbard, 2010; Nouguier et al., 2016), for which a more general model is more appropriate:

$$\sigma_W = \frac{n+2}{n+3}\frac{|R|_T^2}{\cos^4\theta \mathrm{mss}_T\,(n+1)}\left[1+\frac{\tan^2\theta}{\mathrm{mss}_T(n+1)}\right]^{-(n+3)} \tag{A1}$$

Equation 27 is obtained in the limit $n \to \infty$. n is a curvature parameter lying between 1 and 3 in Ku-band (Guimbard, 2010), and mss_T is the total Mean Square Slope, i.e., the one which was measured by Cox and Munk (1954), which inherently differs from $\mathrm{mss}_{\mathrm{eff}}$. Around nominal incidence $\theta = \theta_i$, the function $\psi = \ln\left(\sigma_W \cos^4\theta\right)$ can be expanded around $x_i = \tan^2\theta_i$:

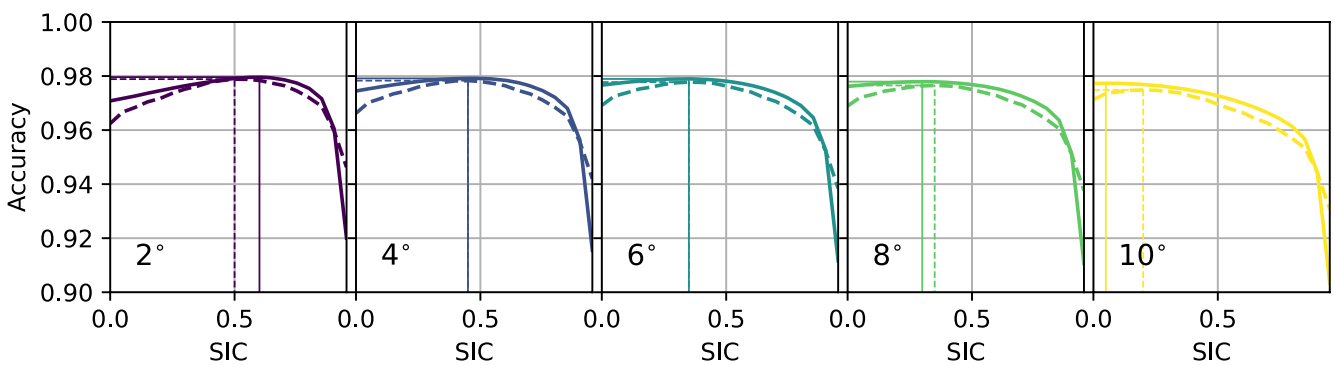

Figure 12. Same as Figure 11 for accuracy, Equation 38. The vertical lines locate the sea-ice concentration (SIC) value corresponding to the maximum accuracy for each reference data set (dashed: ECMWF, solid: SSMI).

Table 8
Values of the Maximum Accuracy and Corresponding SSMI SIC Threshold From Figure 12

Beam	2°	4°	6°	8°	10°
SIC threshold	0.65 (0.55)	0.50 (0.50)	0.35 (0.40)	0.35 (0.40)	0.10 (0.25)
Accuracy (%)	98.0 (97.9)	97.9 (97.9)	97.8 (97.9)	97.8 (97.7)	97.7 (97.5)

Note. The same results with ECMWF SIC are printed in parentheses.

$$\psi(x) \simeq \psi(x_i) + (x - x_i)\, \partial_x \psi|_{x=x_i} \tag{A2}$$

where $x = \tan^2 \theta$. According to geometric optics (Equation 27):

$$\psi \simeq \ln\left(\frac{|R|^2}{\mathrm{mss}_{\mathrm{eff}}}\right) - \frac{x_i}{\mathrm{mss}_{\mathrm{eff}}} - \frac{x - x_i}{\mathrm{mss}_{\mathrm{eff}}}. \tag{A3}$$

Taking curvature effects (Equation A1) into account leads to:

$$\psi \simeq \ln\left(|R|_T^2 \frac{n+2}{\mathrm{mss}_T(n+1)}\right) - (n+3)\ln(1+y_i) - \frac{(x-x_i)(n+3)}{\mathrm{mss}_T(n+1)+x_i} \tag{A4}$$

where $y_i = x_i / [(n+1)\mathrm{mss}_T]$. Equations A3 and A4 lead to

$$\mathrm{mss}_{\mathrm{eff}} \simeq \frac{x_i + (n+1)\mathrm{mss}_T}{n+3} \tag{A5}$$

and

$$|R|^2 \simeq |R|_T^2 \frac{n+2}{n+3}(1+y_i)^{-(n+2)} \exp\left(\frac{n+3}{1+y_i^{-1}}\right) \tag{A6}$$

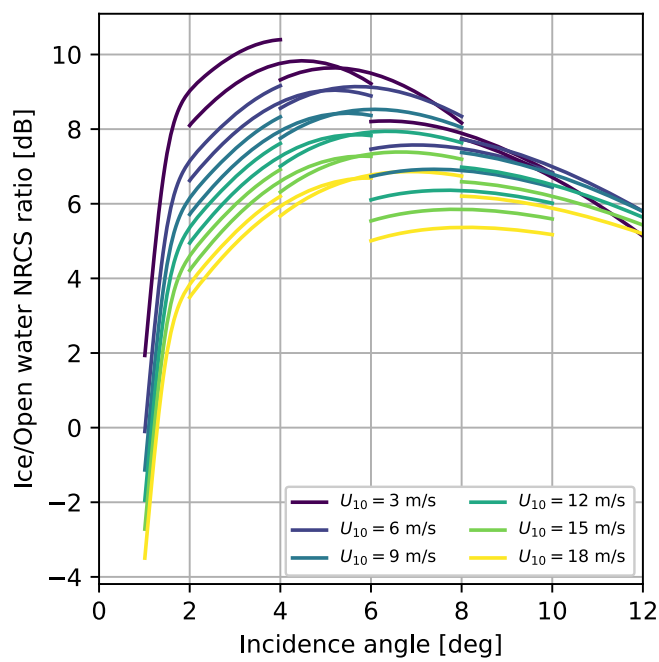

Figure 13. Average sea-ice/open water Normalized Radar Cross-Section (NRCS) ratio in dB from Equation 39 at various wind speeds for SWIM off-nadir beams.

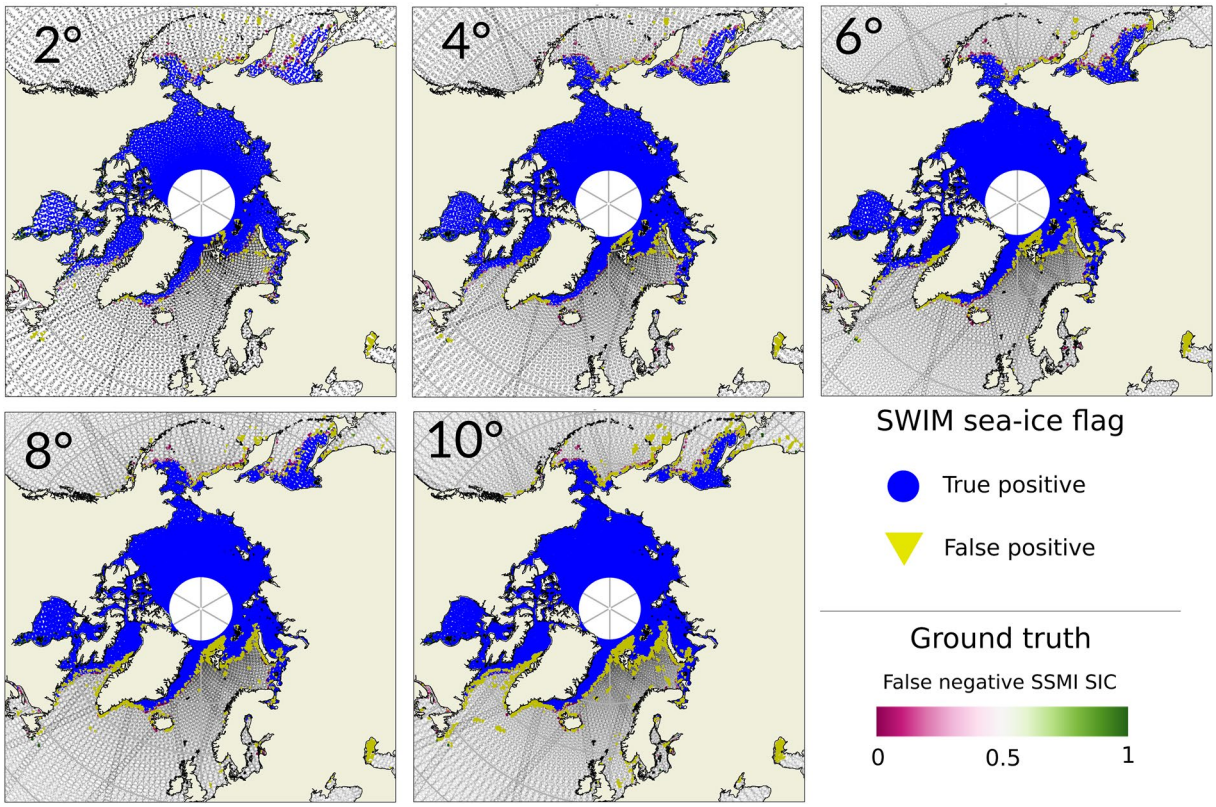

Figure 14. Maps of flagged SWIM profiles location for each beam and comparison with SSMI data with concentrations above 1% around the North pole for cycle 63 (January 2021).

More specifically, the evolution of the effective parameters with nominal incidence θ_i can be deduced:

$$\partial_{x_i} \mathrm{mss}_{\mathrm{eff}} = \frac{1}{n+3} \tag{A7}$$

and

$$\partial_{x_i} |R|^2 = \frac{|R|^2}{(n+1)\mathrm{mss}_T (1+y_i)^2} [1-(n+2)y_i] \tag{A8}$$

As in near-nadir Ku-band $n > 0$ and $y_i \ll 1$, then

$$\partial_{\theta_i} \mathrm{mss}_{\mathrm{eff}} > 0, \tag{A9}$$

and

$$\partial_{\theta_i} |R|^2 > 0. \tag{A10}$$

This trend is indeed the one found in Figure 7 for $\mathrm{mss}_{\mathrm{eff}}$. For $|R|^2$, it is also found in Figure 6 with the exception of beam 2° whose results may be affected by a relative bias in NRCS between the beams.

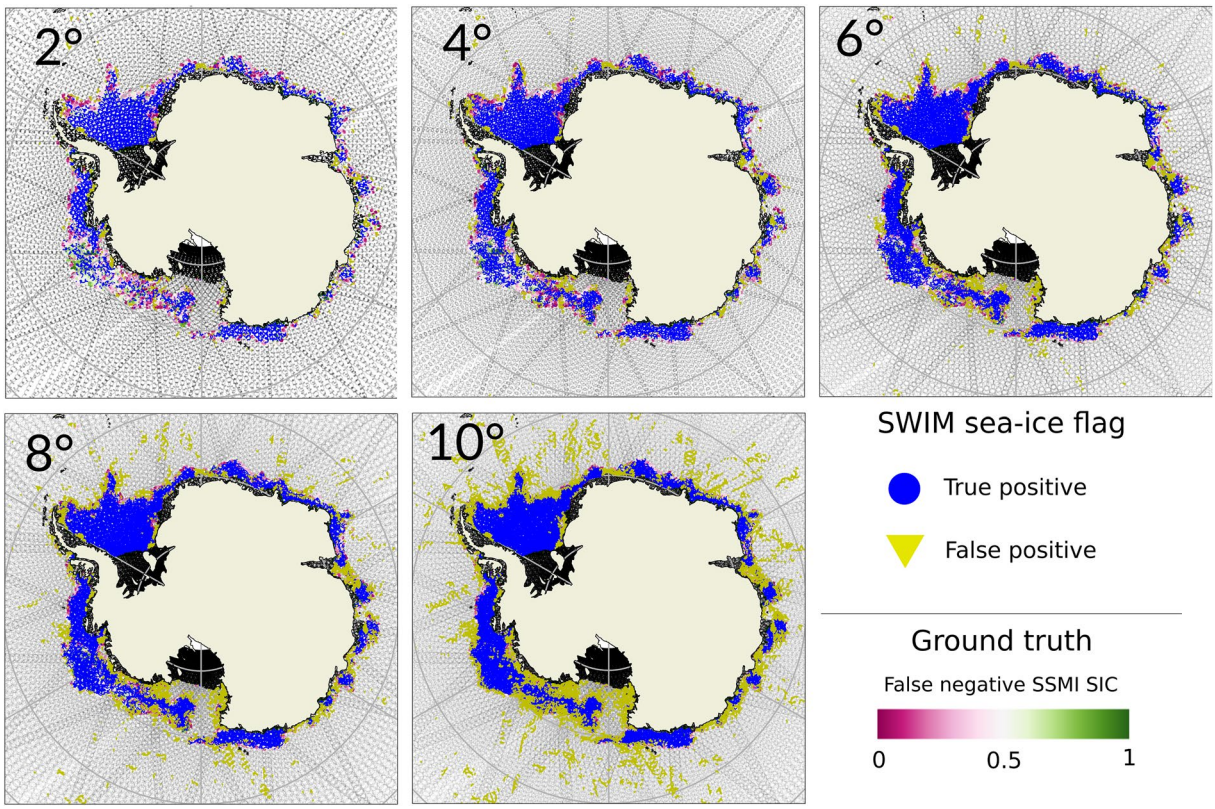

Figure 15. Same as Figure 14 for Antarctica.

Data Availability Statement

All SWIM data used for this study, for example, L1A and auxiliary meteorological files, are freely available upon registration on AVISO + website: https://aviso-data-center.cnes.fr/. Spatiotemporal ranges as well as processing version and variable names are detailed all along the text when needed. Sentinel 1 data are freely available on Copernicus Scihub upon registration: https://scihub.copernicus.eu/. Colocated NRCS map in Figure 10 is obtained from Level 2 file S1b_EW_OCN__2SDH_20201007T202743_20201007T202837_023,711_02D0EF_E580. SAFE without denoising from processing version IPF 3.31. SSMI data for this research are freely available and described in Ezraty et al. (2007). They were accessed upon request to Ifremer CERSAT facility. Sea-ice concentration data sets can be accessed from CERSAT web site: http://cersat.ifremer.fr/oceanography-from-space/our-domains-of-research/sea-ice/radar-backscatter-of-sea-ice.

Acknowledgments
Fanny Girard-Ardhuin and CERSAT Ifremer are greatly acknowledged for their support working with SSMI data. The authors also thank two anonymous reviewers for their attentive proofreading and their pertinent comments, that helped improving the quality of this article.

References

Alhumaidi, S. M., Jones, L., Park, J.-D., & Ferguson, S. M. (1997). A neural network algorithm for sea ice edge classification. *IEEE Transactions on Geoscience and Remote Sensing*, *35*(4), 817–826. https://doi.org/10.1109/36.602524

Barrick, D., & Peake, W. (1968). A review of scattering from surfaces with different roughness scales. *Radio Science*, *3*(8), 865–868. https://doi.org/10.1002/rds196838865

Belmonte Rivas, M., Otosaka, I., Stoffelen, A., & Verhoef, A. (2018). A scatterometer record of sea ice extents and backscatter: 1992–2016. *The Cryosphere*, *12*(9), 2941–2953. https://doi.org/10.5194/tc-12-2941-2018

Belmonte Rivas, M., & Stoffelen, A. (2011). New Bayesian algorithm for sea ice detection with QuikSCAT. *IEEE Transactions on Geoscience and Remote Sensing*, *49*(6), 1894–1901. https://doi.org/10.1109/TGRS.2010.2101608

Belmonte Rivas, M., Verspeek, J., Verhoef, A., & Stoffelen, A. (2012). Bayesian sea ice detection with the advanced scatterometer ASCAT. *IEEE Transactions on Geoscience and Remote Sensing*, *50*(7), 2649–2657. https://doi.org/10.1109/TGRS.2011.2182356

Boisot, O., Nouguier, F., Chapron, B., & Guerin, C. (2015). The GO4 model in near-nadir microwave scattering from the sea surface. *IEEE Transactions on Geoscience and Remote Sensing*, *53*(11), 5889–5900. https://doi.org/10.1109/TGRS.2015.2424714

Breivik, L., Eastwood, S., & Lavergne, T. (2012). Use of c-band scatterometer for sea ice edge identification. *IEEE Transactions on Geoscience and Remote Sensing*, *50*(7), 2669–2677. https://doi.org/10.1109/TGRS.2012.2188898

Chapron, B., Kerbaol, V., Vandemark, D., & Elfouhaily, T. (2000). Importance of peakedness in sea surface slope measurements and applications. *Journal of Geophysical Research*, *105*(C7), 17195–17202. https://doi.org/10.1029/2000JC900079

Chen, P., Zheng, G., Hauser, D., & Xu, F. (2018). Quasi-Gaussian probability density function of sea wave slopes from near nadir Ku-band radar observations. *Remote Sensing of Environment*, *217*, 86–100. https://doi.org/10.1016/j.rse.2018.07.027

Chu, X., He, Y., & Karaev, V. (2012). Relationships between ku-band radar backscatter and integrated wind and wave parameters at low incidence angles. *IEEE Transactions on Geoscience and Remote Sensing*, *50*(11), 4599–4609. https://doi.org/10.1109/TGRS.2012.2191560

Cox, C., & Munk, W. (1954). Measurement of the roughness of the sea surface from photographs of the sun's glitter. *Journal of Optical Society of America*, *44*(11), 838. https://doi.org/10.1364/josa.44.000838

Ezraty, R., Girard-Ardhuin, F., Piollé, J., Kaleschke, L., & Heygster, G. (2007). *Arctic and antarctic sea-ice concentration and arctic sea ice drift estimated from special sensor microwave imager data, user's manual version 2.1* (NASA Tech. Memo. 104647). Greenbelt, MD:Goddard Space Flight Center.

Freilich, M., & Vanhoff, B. (2003). The relationship between winds, surface roughness, and radar backscatter at low incidence angles from TRMM precipitation radar measurements. *Journal of Atmospheric and Oceanic Technology*, *20*(4), 549–562. https://doi.org/10.1175/1520-0426(2003)20<549:TRBWSR>2.0.CO;2

Giles, K., Laxon, S., Wingham, D., Wallis, D., Krabill, W., Leuschen, C., et al., (2007). Combined airborne laser and radar altimeter measurements over the Fram Strait in May 2002. *Remote Sensing of Environment*, *111*(2), 182–194. https://doi.org/10.1016/j.rse.2007.02.037

Girard-Ardhuin, F., & Ezraty, R. (2012). Enhanced arctic sea ice drift estimation merging radiometer and scatterometer data. *IEEE Transactions on Geoscience and Remote Sensing*, *50*(7), 2639–2648. https://doi.org/10.1109/TGRS.2012.2184124

Gressani, V., Nouguier, F., & Mouche, A. (2018). Wave spectrometer tilt modulation transfer function using near-nadir ku- and ka-band GPM radar measurements. In *Igarss 2018-2018 IEEE international geoscience and remote sensing symposium* (pp. 4107–4110). IEEE. https://doi.org/10.1109/IGARSS.2018.8517384

Guerin, C., Poisson, J., Piras, F., Amarouche, L., & Lalaurie, J. (2017). Ku-/ka-band extrapolation of the altimeter cross section and assessment with jason2/AltiKa data. *IEEE Transactions on Geoscience and Remote Sensing*, *55*(10), 5679–5686. https://doi.org/10.1109/TGRS.2017.2711863

Guimbard, S. (2010). *Interprétation et modélisation de mesures à distance de la surface marine dans le domaine micro-onde*.

Hagfors, T. (1970). Remote probing of the moon by infrared and microwave emissions and by radar. *Radio Science*, *5*(2), 189–277. https://doi.org/10.1029/RS005i002p00189

Hauser, D., & Tison, C. (2018). *SWIM products users guide, product description and algorithm theoretical baseline description* (Tech. Rep. No. CF-GSFR-MU-2530-CNES). CNES.

Hauser, D., Tison, C., Amiot, T., Delaye, L., Corcoral, N., & Castillan, P. (2017). Swim: The first spaceborne wave scatterometer. *IEEE Transaction on Geoscience and Remote Sensing*, *55*(5), 3000–3014. https://doi.org/10.1109/tgrs.2017.2658672

Hauser, D., Tourain, C., Hermozo, L., Alraddawi, D., Aouf, L., Chapron, B., & Tran, N. (2021). New observations from the SWIM radar on-board CFOSAT: Instrument validation and ocean wave measurement assessment. *IEEE Transaction on Geoscience and Remote Sensing*, *59*(1), 5–26. https://doi.org/10.1109/TGRS.2020.2994372

Hauser, D., Xiaolong, D., Aouf, L., Tison, C., & Castillan, P. (2016). Overview of the CFOSAT mission. In *IGARSS'16*. IEEE. https://doi.org/10.1109/igarss.2016.7730512

Hossan, A., & Jones, W. (2021). Ku- and ka-band ocean surface radar backscatter model functions at low-incidence angles using full-swath GPM DPR data. *Remote Sensing*, *13*(8), 1569. https://doi.org/10.3390/rs13081569

Johannessen, O., Alexandrov, V., Frolov, I., Sandven, S., Pettersson, L., Bobylev, L., & Babich, N. (2007). *Remote sensing of sea ice in the northern sea route: Studies and applications*. Berlin/Heidelberg, Germany:Springer.

Kaleschke, L., Lüpkes, C., Vihma, T., Haarpaintner, J., Bochert, A., Hartmann, J., & Heygster, G. (2001). SSM/I sea ice remote sensing for mesoscale ocean-atmosphere interaction analysis. *Canadian Journal of Remote Sensing*, *27*(5), 526–537. https://doi.org/10.1080/07038992.2001.10854892

Karaev, V., Panfilova, M., Ryabkova, M., Titchenko, Y., & Meshkov, E. (2021). Remote sensing of sea-ice at small incidence angles: Verification of theoretical models. In *International geoscience and remote sensing symposium* (pp. 5629–5632). IEEE. https://doi.org/10.1109/igarss47720.2021.9554163

Kurtz, N., Farrell, S., Studinger, M., Galin, M., Harbeck, J., Lindsay, R., & Sonntag, J. (2013). Sea ice thickness, freeboard, and snow depth products from operation IceBridge airborne data. *The Cryosphere*, *7*(4), 1035–1056. https://doi.org/10.5194/tc-7-1035-2013

Kurtz, N., Galin, N., & Studinger, M. (2014). An improved CryoSat-2 sea ice freeboard retrieval algorithm through the use of waveform fitting. *The Cryosphere*, *8*(4), 1217–1237. https://doi.org/10.5194/tc-8-1217-2014

Kwok, R. (2004). Annual cycles of multiyear sea ice coverage of the arctic ocean: 1999–2003. *Journal of Geophysical Research*, *109*, C11004. https://doi.org/10.1029/2003JC002238

Landy, J., Tsamados, M., & Scharien, R. (2019). A facet-based numerical model for simulating sar altimeter echoes from heterogeneous sea ice surfaces. *IEEE Transactions on Geoscience and Remote Sensing*, *57*(7), 4164–4180. https://doi.org/10.1109/TGRS.2018.2889763

Lindell, D. B., & Long, D. G. (2016a). Multiyear Arctic ice classification using ASCAT and SSMIS. *Remote Sensing*, *8*(4), 294. https://doi.org/10.3390/rs8040294

Lindell, D. B., & Long, D. G. (2016b). Multiyear Arctic sea ice classification using OSCAT and QuikSCAT. *IEEE Transactions on Geoscience and Remote Sensing*, *54*(1), 167–175. https://doi.org/10.1109/TGRS.2015.2452215

Meier, W. N., & Stroeve, J. (2008). Comparison of sea-ice extent and ice-edge location estimates from passive microwave and enhanced-resolution scatterometer data. *Annals of Glaciology*, *48*, 65–70. https://doi.org/10.3189/172756408784700743

Mouche, A., Tournadre, J., Paul, F., Girard-Ardhuin, F., Queffeulou, P., & Longepe, N. (2015). *Global Precipitation Mission, an opportunity for ocean surface remote sensing?* Retrieved from http://www.ifremer.fr/cerweb/amouche/docs/presentations/CNES_Atelier_Glacio/GPM_sea_ice.pdf

Nouguier, F., Mouche, A., Rascle, N., Chapron, B., & Vandemark, D. (2016). Analysis of dual-frequency ocean backscatter measurements at ku-and ka-bands using near-nadir incidence GPM radar data. *IEEE Geoscience and Remote Sensing Letters*, *13*(9), 1310–1314. https://doi.org/10.1109/LGRS.2016.2583198

Otosaka, I., Belmonte Rivas, M., & Stoffelen, A. (2018). Bayesian sea ice detection with the ERS scatterometer and sea ice backscatter model at c-band. *IEEE Transactions on Geoscience and Remote Sensing*, *56*(4), 2248–2254. https://doi.org/10.1109/TGRS.2017.2777670

Panfilova, M., Shikov, A., & Karaev, V. (2020). Sea ice detection using Ku-band radar onboard GPM satellite. In *2020 XXXIIIrd URSI general assembly and scientific symposium of the international union of radio science* (pp. 1–3). IEEE. https://doi.org/10.23919/URSIGASS49373.2020.9232361

Remund, Q., & Long, D. (2003). Large-scale inverse ku-band backscatter modeling of sea ice. *IEEE Transactions on Geoscience and Remote Sensing*, *41*(8), 1821–1832. https://doi.org/10.1109/TGRS.2003.813495

Ren, L., Yang, J., Xu, Y., Zhang, Y., Zheng, G., Wang, J., & Jiang, J. D. C. (2021). Ocean surface wind speed dependence and retrieval from off-nadir CFOSAT SWIM data. *Earth and Space Science*, *8*(6), 1–15. https://doi.org/10.1029/2020EA001505

Shokr, M., & Sinha, N. (2015). *Sea ice: Physics and remote sensing*. American Geophysical Union. https://doi.org/10.1002/9781119028000.ch5

Swift, C. (1999). Seasat scatterometer observations of sea-ice. *IEEE Transactions on Geoscience and Remote Sensing*, *37*(21), 716–723. https://doi.org/10.1109/36.752188

Tournadre, J., Whitmer, K., & Girard-Ardhuin, F. (2008). Iceberg detection in open water by altimeter waveform analysis. *Journal of Geophysical Researchs*, *113*, C08040. https://doi.org/10.1029/2007JC004587

Tran, N., Chapron, B., & Vandemark, D. (2007). Effect of long waves on ku-band ocean radar backscatter at low incidence angles using TRMM and altimeter data. *IEEE Geoscience and Remote Sensing Letters*, *4*(4), 542–546. https://doi.org/10.1109/LGRS.2007.896329

Xiaolong, D., Di, Z., Lin, W., Liu, H., & Jiang, J. (2010). A ku-band rotating fan-beam scatterometer: Design and performance simulations. In *IGARSS'10* (pp. 1081–1084). IEEE. https://doi.org/10.1109/IGARSS.2010.5650797

Yan, Q., Zhang, J., Fan, C., & Meng, J. (2019). Analysis of ku- and ka-band sea surface backscattering characteristics at low-incidence angles based on the GPM dual-frequency precipitation radar measurements. *Remote Sensing*, *11*(7), 754. https://doi.org/10.3390/rs11070754

Zhang, Z., Yu, Y., Li, X., Hui, F., Cheng, X., & Chen, Z. (2019). Arctic sea ice classification using microwave scatterometer and radiometer data during 2002–2017. *IEEE Transactions on Geoscience and Remote Sensing*, *57*(8), 5319–5328. https://doi.org/10.1109/TGRS.2019.2898872